R. Tyagi, and S. Srinivasan

View Online   Export Citation   CrossMark

ARTICLES YOU MAY BE INTERESTED IN

Molecular dynamics modeling of lithium ion intercalation induced change in the mechanical properties of $Li_xMn_2O_4$

View Online   Export Citation   CrossMark

R. Tyagi[1] (ID) and S. Srinivasan[1,2,a] (ID)

AFFILIATIONS

[1] Department of Mechanical Engineering, McMaster University, Hamilton, Ontario L8S 4L8, Canada
[2] W Booth School of Engineering Practice and Technology, McMaster University, Hamilton, Ontario L8S 4L8, Canada

[a] Author to whom correspondence should be addressed: ssriniv@mcmaster.ca

ABSTRACT

The objective of this study is to understand the fracture mechanisms in the lithium manganese oxide ($LiMn_2O_4$) electrode at the molecular level by studying mechanical properties of the material at different values of the State of Charge (SOC) using the principles of molecular dynamics (MD). A $2 \times 2 \times 2$ cubic structure of the $LiMn_2O_4$ unit cell containing eight lithium ions, eight trivalent manganese ions, eight tetravalent manganese ions, and 32 oxygen ions is studied using a large-scale atomic/molecular massively parallel simulator. As part of the model validation, the lattice parameter and volume changes of $Li_xMn_2O_4$ as a function of SOC ($0 < x < 1$) have been studied and validated with respect to the experimental data. This validated model has been used for a parametric study involving the SOC value, strain rate (charge and discharge rate), and temperature. The MD simulations suggest that the lattice constant varies from 8.042 Å to 8.235 Å during a full discharging cycle, in agreement with the experimental data. The material at higher SOC shows more ductile behavior compared to low SOC values. Furthermore, yield and ultimate stresses are less at lower SOC values except when SOC values are within 0.125 and 0.375, verifying the phase transformation theory in this range. The strain rate does not affect the fully intercalated material significantly but seems to influence the material properties of the partially charged electrode. Finally, a study of the effect of temperature suggests that diffusion coefficient values for both high and low-temperature zones follow an Arrhenius profile, and the results are successfully explained using the vacancy diffusion mechanism.

Published under license by AIP Publishing. https://doi.org/10.1063/5.0020823

I. INTRODUCTION

Due to their higher theoretical and practical energy density, lithium ion batteries are attractive power sources for portable consumer electronic applications, Hybrid Electric Vehicles (HEVs), and Electric Vehicles (EVs).[1] A lithium ion battery is a rechargeable type of battery that has four primary components, namely, a cathode (lithium metal oxide or positive electrode), an anode (graphite/silicon or negative electrode), a separator (porous polymer), and an organic electrolyte. The separator separates the positive and negative electrodes while allowing ions to pass through. The anode, cathode, and the separator are submerged in an electrolyte solution. During the operation of the battery, the lithium ions migrate between the anode and the cathode. Specifically, during

charging, lithium ions move through the electrolyte from the cathode to anode, while the electrons flow through the external circuit. This mobility is reversed while discharging.

A significant amount of current research is focused on $LiMn_2O_4$ as a cathode material for lithium ion batteries.[2-6] $LiMn_2O_4$ is preferred as a cathode material over others, such as lithium cobalt oxide ($LiCoO_2$) and lithium nickel oxide ($LiNiO_2$), because of its low cost, high operating voltage, higher energy density, and low toxicity.[7,8]

However, this is a challenging material to work with because it shows a large volume change during lithium ion intercalation and de-intercalation processes. Specifically, these processes induce stresses, which can initiate fracture inside the material,[9-11] a key degradation mechanism in the lithium ion batteries.[12-15] It must

be noted that stress is strongly dependent on the lithium content in the electrode.[16] Extensive macrolevel mathematical and computational work has been done to study the mechanical properties of Mn_2O_4 as a host material on lithiation, mostly focusing on Young's modulus that varies quite a bit (10 GPa–200 GPa) across the literature for $LiMn_2O_4$.[11,12,15,17] Molecular and atomistic simulations can provide better understanding of the variations in such mechanical properties due to the lithium ion intercalation and de-intercalation process.

The movement of lithium ions within the cathode material is dictated by the diffusion coefficient of the electrode material. The value of the diffusion coefficient will vary with state of charge (SOC) values, as the availability of the vacant sites changes. Therefore, studying the transition of lithium ions at the molecular level will improve our understanding of the material's response during charging and discharging processes. Additionally, it is important to note that as the temperature inside the cell increases, the energy level will also increase, facilitating a faster diffusion of the ions. Thus, there is an increase in the overall diffusion coefficient for these ions. Currently, research work that focuses on temperature influence on lithium ion diffusivity at various SOC values for $Li_xMn_2O_4$ is limited in the literature and there is a significant variation in the diffusivity values.[11,12,15,17] Furthermore, it is very difficult to perform precise experiments at the molecular level. This is evident from the wide range of diffusion coefficients values at room temperature (10^{-8} cm^2/s to 10^{-15} cm^2/s) that have been reported in the literature using the different experimental methods.[18–20] This is because the transport and other properties depend strongly on the preparatory procedures, which influence the micro structure, defects, and atomic structure of the $LiMn_2O_4$.

To address this shortfall, in addition to the impact of SOC on the diffusion coefficient, influence of the elevated temperature on the structure of $Li_xMn_2O_4$ will be studied in this article. Furthermore, the charge and discharge rates (strain-rates) are also investigated as part of the parametric study in the strain-rate section. The rest of this article is organized as follows. In Sec. II, we describe the details of the molecular dynamics (MD) simulations, including the analysis of the effect of the cutoff length. In this section, we also outline the theoretical framework for the analysis of the mechanical properties and the diffusion coefficient. In Sec. III, we present the validation of the computational tool and the outcome of the parametric analysis. Finally, we present the main conclusions from our findings.

II. COMPUTATIONAL TOOLS

Molecular dynamics (MD) simulations have been used to calculate the mechanical properties of the $Li_xMn_2O_4$. MD simulations have been preferred over other types of numerical modeling of chemical physics problems because they can capture the dynamic behavior of the ions and can help us understand the underlying physics at a molecular scale. The ensuing paragraphs describe the simulation tool in detail.[21–23]

A. Molecular dynamics simulations

Interactions between various ions determine the potential, which is responsible for atomic movement, that will eventually

TABLE I. Parameters for the potential function.

Ion	Z_i	a_i (Å)	b_i (Å)
Li$^+$	+1.0	1.043	0.080
Mn^{3+}	+1.4	1.038	0.070
Mn^{4+}	+2.4	0.958	0.070
O^{2-}	−1.2	1.503	0.075

govern the mechanical and chemical properties. In this work, the Gilbert–Ida-type pair potential function[24] has been used to calculate the inter-atomic pair potentials as

$$E = \frac{Z_i Z_j e^2}{r_{ij}} + A_{ij} \exp\left(\frac{\sigma_{ij} - r_{ij}}{\rho_{ij}}\right) \quad for \quad r_{ij} < r_c, \quad (1)$$

where the first term represents the electrostatic interactions and the second term represents the exchange repulsion interactions. Z_i and Z_j are the atomic charges of atoms i and j, respectively, and r_{ij} is distance between atoms/charges. Furthermore, σ_{ij} is an interaction-dependent length parameter, ρ_{ij} is an ionic-pair dependent length parameter, r_c is the cutoff length, and e is the elementary electric charge. Potential function parameters reported by Suzuki et al.,[25] and as summarized in Table I, are used to calculate the values of A_{ij}, σ_{ij}, and ρ_{ij} for each pair interaction, where $\rho_{ij} = b_i + b_j$, $A_{ij} = f_0 \times \rho_{ij}$, $\sigma_{ij} = a_i + a_j$, and f_0 is a constant.

A unit cell of $LiMn_2O_4$ contains 56 ions (eight Li$^+$, eight Mn^{3+}, eight Mn^{4+}, and 32 O^{2-}), and these ions are in a cubical structure in the Fd3m space group. The atomic coordinates of these 56 particles were taken from a study performed by Sickafus et al.[26]

1. Cutoff length

From Eq. (1), it is clear that inter-atomic pair potential depends upon the cutoff length, beyond which the interaction potential can be neglected. While increasing the cutoff length will improve the accuracy of the solution, there is a significant increase in the computational cost. To understand the trade-off between accuracy and cost and to choose an optimal cutoff length, three different cutoff lengths (6 Å, 8 Å, and 10 Å) have been considered. More precisely, MD simulations were performed for two different SOC values, i.e., SOC = 1 and SOC = 0.5, using the three cutoff lengths for each SOC value. The results from these simulations are shown in Figs. 1 and 2, respectively. As shown in Fig. 1, the effect of either of these cutoff lengths on the variations in the stress–strain relationship is minimal. This is because when SOC = 1, the number of vacant sites is minimal, and so, the diffusion activity is largely subdued. Hence, for this situation, a lower cutoff length would still produce a fairly accurate result.

Figure 2 shows the results of the MD simulations when SOC = 0.5. As shown in this figure, the stress–strain relationship predicted by the cutoff lengths of 6 Å or 10 Å is quite similar. However, the computational time for the 10 Å case is ~1.5 times longer than the 6 Å case. When the cutoff length is 8 Å, we notice some insignificant variations in the stress–strain relationship. Hence, keeping in mind
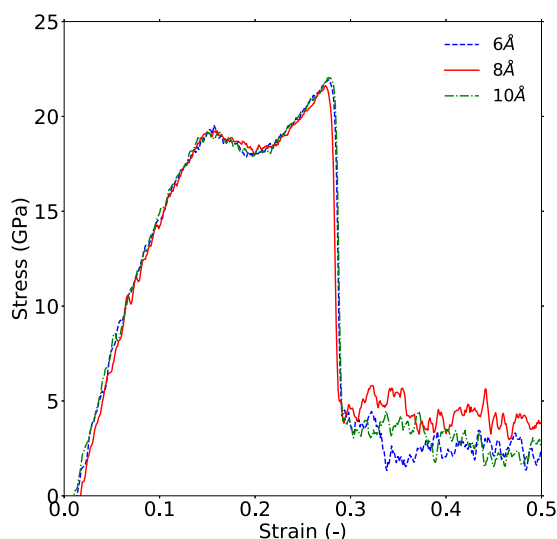
FIG. 1. Stress–strain curve for different cutoff lengths at SOC = 1.

FIG. 2. Stress–strain curve for different cutoff lengths at SOC = 0.5.
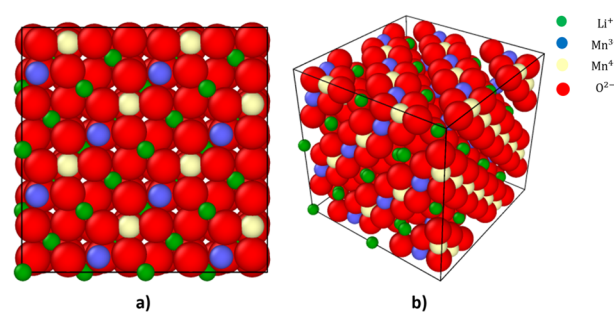
FIG. 3. LiMn$_2$O$_4$ simulations box: (a) front view and (b) 3D view.

the boundary effects on the solution and computational cost, in this work, the cutoff length was chosen as 10 Å for all the MD simulations. We believe that increasing the cutoff length any further is not likely to improve the accuracy of the calculations significantly.

It must be noted that this cutoff distance of 10 Å is greater than the size of a unit cell, which is 8.24 Å. Therefore, a minimum of two-unit cells are required to perform MD simulations. However, increasing the number of unit cells results in a larger simulation box, which will increase the computational load and thereby the cost. Hence, in all the simulations of this work, we have used a 2 × 2 × 2
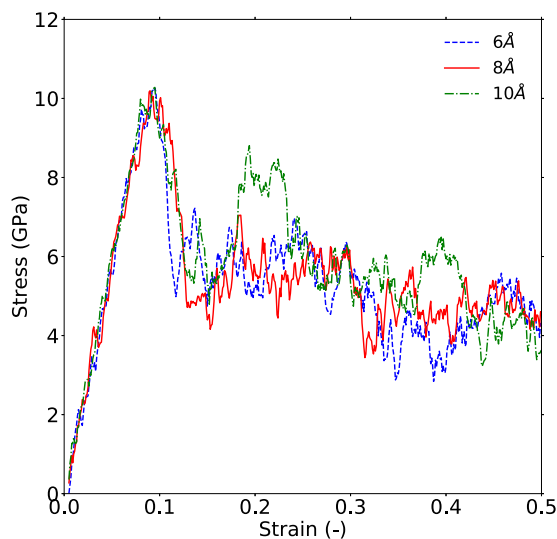
simulation box in x, y, and z-directions, respectively. The front view and the three-dimensional view of the 2 × 2 × 2 simulation box are shown in Fig. 3.

All MD simulations are performed using LAMMPS (Large-scale Atomic/Molecular Massively Parallel Simulator)[27] open source-based software, which is a classical molecular dynamics code. To calculate the inter-atomic potential described in Eq. (1), it is transformed into the Buckingham potential available in LAMMPS.[28,29] The Ewald method is used for computing the long-range Coulombic interactions.[30] The isothermal isobaric (NPT) ensemble is used during equilibrium and production processes, and a canonical ensemble (NVT) is used for strain simulations. For the NPT ensemble, the number of particles, pressure, and temperature of the simulation box is kept constant. On the other hand, for the NVT ensemble, the volume along with the number of particles and temperature are kept constant. The Nose–Hoover thermostat has been used to regulate the system's temperature at specific temperatures.[31]

Simulations are performed in two stages: first, optimized structures are found by running initial configurations for one-time step, and four cases with the least potential energies are subsequently equilibrated along with the production simulations. An average of the data from these cases is presented as the final result. Furthermore, based on the SOC values, there are nine possible scenarios corresponding to the number of lithium ions in the system that can vary from 0 to 8. The corresponding SOC values vary from 0 to 1 with an increment by 0.125 for each additional lithium ion. As the number of lithium ions increase, an equivalent number of Mn^{4+} switch to Mn^{3+} sites to maintain system's neutrality.

All lithium ions are positioned on the 8a tetrahedral sites, manganese (Mn^{3+} and Mn^{4+}) are placed at 16d octahedral sites, and O^{2-} are located at the 32e sites. Due to the complexity of the LiMn$_2$O$_4$ structure, numerous initial configurations are possible as the ion occupies one of these positions. For example, in a fully discharged state, when lithium ions intercalate into Li$_x$Mn$_2$O$_4$ (x = 1), the number of possible cases in which Li$^+$, Mn^{3+}, and Mn^{4+} could be arranged in the vacant sites would be 12 870. Similarly, for other SOC values, there will be numerous potential configurations, as summarized in Table II.

As shown in Table II, there is a total of 735 471 possible initial configurations that could be optimized. However, checking equilibrium energy for all these cases would not be computationally

TABLE II. Possible $Li_xMn_2O_4$ configuration for each SOC.

SOC	No. of Li+ ions	Possible configurations
0.000	0	1
0.125	1	128
0.250	2	3 360
0.375	3	31 360
0.500	4	127 400
0.625	5	244 608
0.750	6	224 224
0.875	7	91 520
1.000	8	12 870

feasible. Therefore, initially, a one-step MD simulation is performed for all cases. Since a configuration with the lowest potential energy will have a higher probability of reaching an equilibration state quicker, four lowest potential energy cases from these simulations were picked for longer equilibration simulation. Finally, after equilibration of these four cases, the three cases with the lowest energy were selected for further production and analysis.

B. Mechanical properties

1. Linear elastic relationship

Stress is mainly calculated in the form of virial stress. Stress for a particular SOC structure has been calculated with LAMMPS[32] using the following equation:

$$\sigma(r) = \frac{1}{\Omega} \sum_i \left[-m_i \dot{u}_i \otimes \dot{u}_i + \frac{1}{2} \sum_{j \neq i} r_{ij} \otimes f_{ij} \right], \quad (2)$$

where Ω is the total volume, m_i is the mass of the atom i, $\dot{u}_i$ is the time derivative of u_i, which represents the displacement vector of atom i from reference position r_{ij}, and f_{ij} is the inter-atomic force applied on atom i by atom j. Young's modulus can be calculated from the stress results and analyzed with respect to SOC. The linear elastic stress–strain relationship during an axial test can be calculated using the following relation:[33]

$$\begin{pmatrix} \sigma_{11} \\ \sigma_{22} \\ \sigma_{33} \end{pmatrix} = \begin{pmatrix} C_{11} & C_{12} & C_{13} \\ C_{21} & C_{22} & C_{23} \\ C_{31} & C_{32} & C_{33} \end{pmatrix} \begin{pmatrix} \varepsilon_{11} \\ \varepsilon_{22} \\ \varepsilon_{33} \end{pmatrix}, \quad (3)$$

where σ_{ij}, C_{ij}, and ε_{ij} are the stress, elastic constant, and strain, respectively. The elastic bulk modulus K can be calculated as

$$K = \frac{1}{3}\left(\frac{\sigma_{11} + \sigma_{22} + \sigma_{33}}{\varepsilon_{11} + \varepsilon_{22} + \varepsilon_{33}} \right). \quad (4)$$

Finally, the effective Young's modulus can be evaluated using Eqs. (3) and (4) as

$$E = \frac{9K(C_{11} - K)}{3K + C_{11}}. \quad (5)$$

2. Stress strain-rate

Since chemical and mechanical properties of the cathode material such as $LiMn_2O_4$ are strongly coupled, it is important to understand how the C-rate (charge or discharge rate) influences the mechanical properties of the material. As mentioned earlier, mechanical stresses are induced with the expansion and contraction of the micro-structure during the charging and discharging processes. To measure this quantitatively, we can convert the charging rate into a strain rate using the Vegard relation as follows:[34,35]

$$\varepsilon_c = \beta_{ij}\Delta X, \quad (6)$$

where ΔX is the change in lithium concentration and β_{ij} is the Vegard constant. Since the strain-rate will change with lithium ion concentration, the stress value calculated using Eq. (2) will also change. From Eq. (2), it is clear that the ultimate and tensile stresses will be affected by the change in lithium concentration. Therefore, the strain rate will have a direct impact on the material properties.

C. Lithium ion diffusion

With an increase in temperature, the kinetic energy of the system and thereby the total energy of the system increase. Furthermore, ionic movement will also increase, enhancing thermal diffusivity. As evident from Eq. (7), the chemical diffusion coefficient will also change with the state of the charge, temperature, and other parameters,

$$D(X) = D_0 X(1 - X)\left(-\frac{zF}{RT}\frac{\partial V(X)}{\partial X} + \frac{2\Omega^2 E c_{max}}{9RT(1 - v)} \right), \quad (7)$$

where D_0, X, F, V, Ω, c_{max}, E, and v are the diffusivity coefficient, lithium concentration, Faraday constant, potential, partial molar volume of lithium, maximum lithium concentration, Young's modulus, and Poisson's ratio, respectively.

To understand the influence of the temperature, multiple MD simulations were performed at various temperatures, and the corresponding diffusion constants were calculated using the Mean Square Displacement (MSD) of all the particles in the following formula:

$$MSD(t) = \overline{|r(t) - r(t_0)|^2}, \quad (8)$$

where r(t) and $r(t_0)$ represent the atom coordinates at time t and t_0, respectively. In Eq. (8), the over-line shows the average over the same type of species. The diffusion coefficient of the lithium ion can be determined from MSD values using the following Einstein equation:

$$D = \frac{1}{6} \lim_{t \to \infty} \frac{d}{dt}MSD. \quad (9)$$

III. RESULTS AND DISCUSSION

A. Validation of the computational tool

To ensure the validity of the simulation results, the lattice parameter for the optimized $LiMn_2O_4$ structure at 300 K is calculated. The lattice constant was calculated by measuring the size of

the equilibrated system and is shown in Fig. 4 for various SOC values. As seen in this figure, there is a good agreement between the simulation results and the experimental data.[36,37]

More precisely, the lattice constant varies from 8.042 Å (at x = 0) to 8.235 Å (at x = 1) as we move from a fully charged state to a fully discharged state. The total change in the lattice length and volume during full charging cycle was 2.34% and 6.87%, respectively. It must be noted that this predicted volume change is in excellent agreement with the experimental value of 6.85% presented by Park *et al.*[17]

For additional validation of the simulation tool, the lithium ion diffusion coefficient at various temperatures of $LiMn_2O_4$ has been compared with the experimental data from the literature and is shown in Fig. 5. As shown in this figure, the calculated diffusion coefficients, at various temperatures, are in good agreement with the experimental data of Takai *et al.*[20] and Kuwata *et al.*[19] Specifically, the agreement is very good for a temperature in the range of 573 K–1000 K. At temperatures below 573 K, the diffusion process slows down significantly, and so, the simulation duration was increased from 2 ns to 5 ns. Kuwata *et al.*[19] extrapolated their experimental data and predicted a diffusion coefficient ($\sim 10^{-15}$ cm^2/s) at 298 K that is several orders of magnitude lower than the chemical diffusion coefficient ($\sim 10^{-12}$ cm^2/s). On the other hand, the simulations from this work, using the principles of molecular dynamics, predict the diffusion coefficient as $\sim 7.4 \times 10^{-11}$ cm^2/s, and this value is well within the range of chemical diffusion coefficients at 300 K.[38]

The MD tool that is successfully validated with the experimental data has been used to conduct a parametric study. Specifically, three parameters have been investigated in this work, namely, the state of charge, strain rate, and the temperature. From Eq. (1), it is clear that the output potential that is dependent on pair interactions is governed by the lithium content in the cathode material. As the number of lithium ions increases, the SOC value changes,
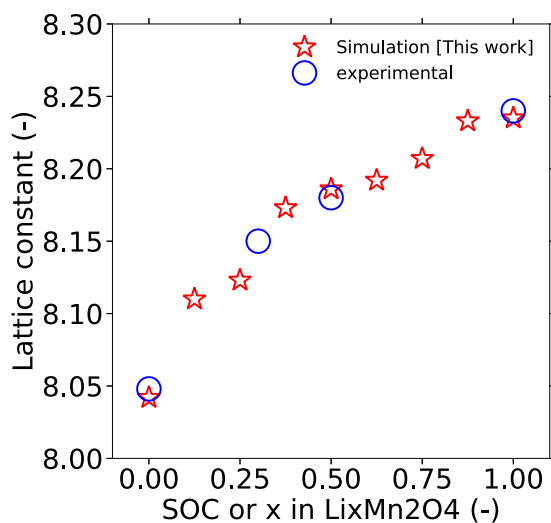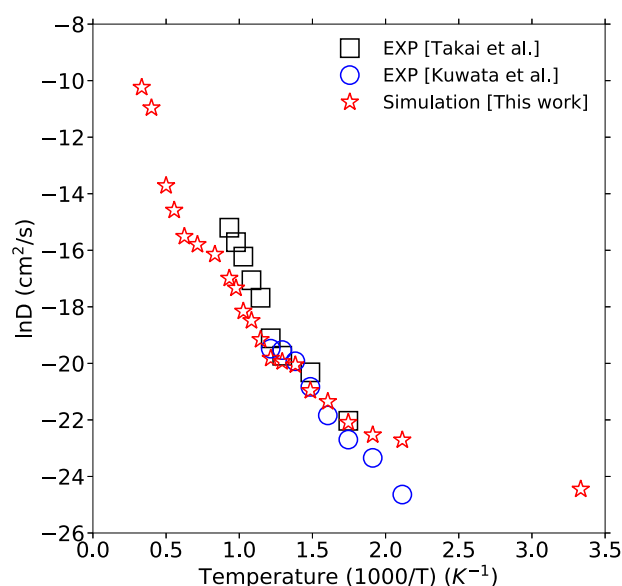

FIG. 5. Lithium ion diffusion coefficient validation with experiments.

impacting the material property. Therefore, SOC is an important parameter to study. Since in almost all intercalation materials such as $LiMn_2O_4$, the intercalation induced fracture mechanism is active especially at high charge or discharge rates, it is necessary to study influence of the strain-rate on mechanical properties of the material.[39] Finally, as the temperature increases, ions will start moving quicker, increasing the kinetic energy of the system and thereby the total stress and diffusivity of the lithium ions.[40] Therefore, temperature has been chosen as the third parameter to be investigated in this study, especially for different SOC states. The cutoff length range is another input parameter that can influence the potential value and thereby impact the calculations, making it an important parameter to investigate. We have investigated this to ensure that an optimal cutoff length is used in our MD simulations, as presented in Sec. II.

1. State of charge (SOC)

Pair interactions are a major cause for the changes in the stress development in the cathode material. During insertion and extraction (electrochemical cycling) of the lithium ions, the number of Li^+, Mn^{3+}, and Mn^{4+} in the material changes, affecting the interactions between these ions. These variations in the pair interaction in turn affect the mechanical properties of the cathode material.[41] Put differently, the elastic properties of the $Li_xMn_2O_4$ cathode material vary with the state of charge. To study this, uni-axial deformation in the x-direction has been performed by applying 0.5% of strain at the C/2 discharge rate.

Figure 6 shows the stress–strain curve for different SOC values. As seen in this figure, there is a strong relationship between SOC and the stress–strain behavior of the material. Initially, the relationship is almost linear, indicating an elastic behavior. In the case of $LiMn_2O_4$, the stress curve exhibits non-linearity after a strain of ~0.1, reaching
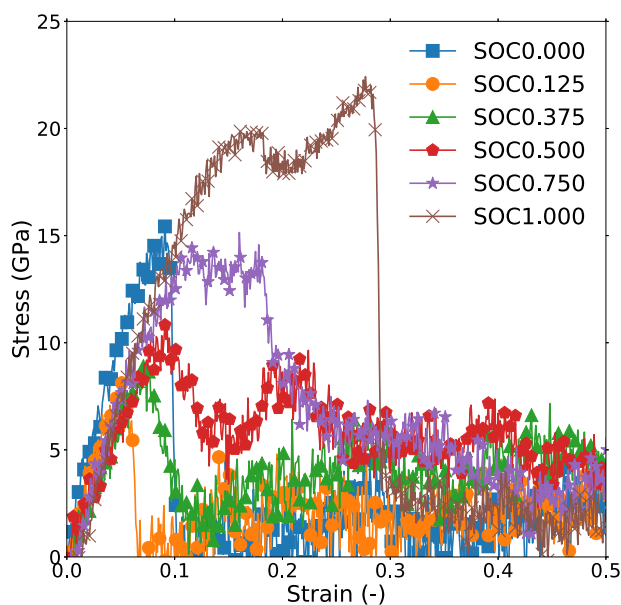

FIG. 4. Lattice parameter with SOC.

FIG. 6. Stress–strain curve for each SOC value at the 0.01 ps^{-1} strain rate.

FIG. 7. Young's modulus for various state of charges.

the maximum stress of ~22 GPa at a strain of around 0.275. After attaining this peak, the stress values decreased sharply, indicating an initiation of fracture. A comparison of the stress–strain curves at different SOC values shows that as the amount of Li decreases, the peak stress values decline. This is because of the change in the lattice structure for different SOC values.

Unlike LiMn$_2$O$_4$, in Li$_{0.375}$Mn$_2$O$_4$, Li$_{0.5}$Mn$_2$O$_4$, and Li$_{0.75}$Mn$_2$O$_4$, after reaching the peak values, the stress does not drop immediately. Instead, we observe a large fluctuation. During the first decrease in the curve, amorphization due to atomic slip spreads out from the hole in the horizontal direction. During the second decrease in the curve, void nucleation and growth were observed inside of the amorphous region. These plastic behaviors are more pronounced at a lower concentration of Li.

From Fig. 6, it is not difficult to conclude that the yield and ultimate stress values will vary with SOC values, yield stress being the point after which plastic deformation starts, and ultimate stress being the maximum stress value in the stress–strain curve. It can also be seen that in the early stages of charging (higher SOC values), the material shows a more ductile behavior, whereas toward the end of the charging stage (lower SOC), it becomes more brittle, with the plastic behavior disappearing almost entirely. For SOC values in the range of 0–0.375, the initial stress values rise quite rapidly. This can be attributed to the presence of more than one phase in this range of SOC values, as has been reported in the literature.[12]

As a further validation of our results, in this work, Young's modulus at various SOC values has been calculated using Eq. (5), following the averaging approach suggested by Lee et al.[41] As can be seen in Fig. 7, there is a good agreement with the data reported in the literature.[41,42] The value of Young's modulus decreases from $x = 0$ to $x = 0.250$, varying from 163 GPa to 140 GPa. Furthermore, it increases from $x = 0.375$ to $x = 1$, varying from 147 GPa to 160 GPa.
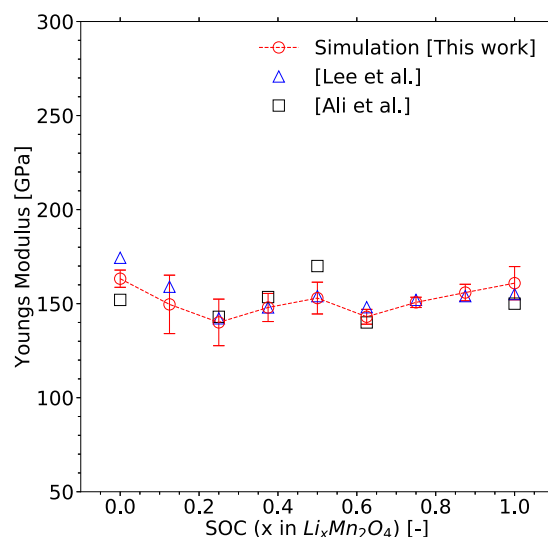
The variation in Young's modulus can be explained as follows: The mechanical properties of LiMn$_2$O$_4$ could be affected by three terms: the kinetic energy contribution, the long-range Coulombic interactions, and the pair interactions. The kinetic energy contribution and long-range Coulombic interactions do not change during the electrochemical charge cycle and therefore do not have any effect on the mechanical properties. Pair interactions are the only responsible phenomenon for the changes in the mechanical properties during electrochemical cycling. There are ten types of pair-interactions in the LiMn$_2$O$_4$ system: Li$^+$–Li$^+$, Li$^+$–Mn^{3+}, Li$^+$–Mn^{4+}, Li$^+$–O^{2-}, Mn^{3+}–Mn^{3+}, Mn^{3+}–Mn^{4+}, Mn^{3+}–O^{2-}, Mn^{4+}–Mn^{4+}, Mn^{4+}–O^{2-}, and O^{2-}–O^{2-}. During charging and discharging processes, numbers of these ions and their interactions change, affecting the mechanical properties, including Young's modulus. This is consistent with the propositions of Lee et al.[41]

2. Strain rate

In studying the mechanical properties of the Li$_x$Mn$_2$O$_4$, it is important to understand the development of stress inside the material at different charging or discharging rates (C-rate). To this end, in this work, MD simulations for three different strain rates (0.001 ps^{-1}, 0.01 ps^{-1}, and 0.1 ps^{-1}) at two different SOC values (1 and 0.5) have been performed. These strain rates correspond to C-rates of 0.5 C, 5 C, and 50 C, respectively. The stress–strain curves for these simulations are shown in Fig. 8 for SOC = 1 and Fig. 9 for SOC = 0.5.

As shown in Fig. 8, the strain-rate seems to have a negligible effect on the elastic properties of the material, at least for LiMn$_2$O$_4$ (SOC = 1). It has also been observed in the work of Woodford et al.[43]

On the other hand, the trend is different when SOC = 0.5 (cf. Fig. 9). In this partially charged case, the yield stress and the ultimate stress increase by 70% as we go from a strain rate of 0.1 ps^{-1}
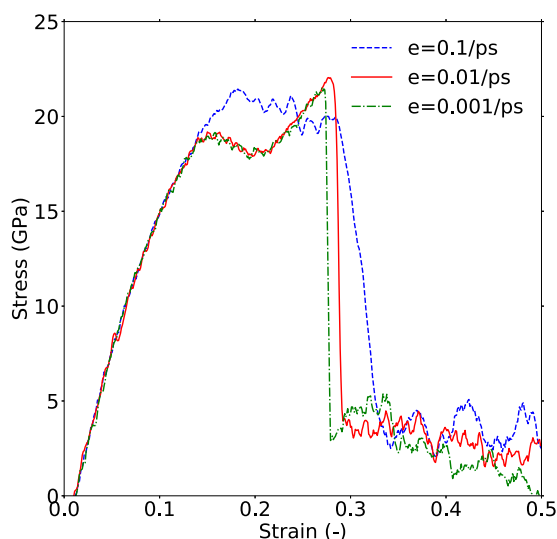
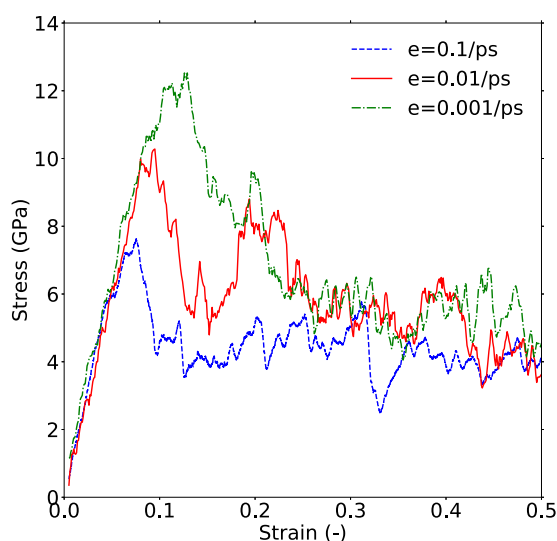**FIG. 8**. Stress–strain curve for different strain rates at SOC = 1.

FIG. 9. Stress–strain curve for different strain rates at SOC = 0.5.

to 0.001 ps^{-1}. This is a clear indicator that the elastic properties such as Young's modulus changes with the strain rate. This change in the elastic properties can be attributed to the pair interaction response to different strain-rates, which determines the mechanical properties.

3. Temperature

Diffusion property has a significant influence on the performance of Li-ion batteries. However, most of the investigations in the literature have been restricted to the measurement of the lithium ion diffusion coefficient experimentally due to the very light nature

of the element and lack of a widely accepted radioisotope for the lithium ion.[44] Additionally, there is a lack of experimental and theoretical consensus on the effect of stoichiometry on the diffusion properties during the charging and discharging processes when there are considerable variations in the lithium vacancy concentration. In this subsection, we investigate the diffusion of lithium in spinel $Li_xMn_2O_4$ phases through MD simulations. MD simulations are carried out over a temperature range of 300 K–3000 K. Each simulation is for a duration of 20 ps during equilibration and another 2 ns for the analysis of the ionic displacement.

Figure 10 shows the variation in the diffusion coefficient as a function of temperature, capturing the magnitude of the Li-ion diffusion inside the cathode material with variation in temperature. The trend in this figure is consistent with the findings in the literature.[45] As shown in this figure, in the high temperature zone (T > 823 K), the diffusion coefficients are quite close across all SOC values. However, in the low temperature zone (473 K < T < 823 K), at lower SOC values, the diffusion coefficient is much higher than the diffusion coefficients at the SOC value closer to stoichiometry. This can be explained by the fact that at lower SOC values, the number of vacant sites is higher, reducing the energy barrier for the ions to diffuse. In general, the diffusion coefficient for a fully discharged and charged state at 300 K will vary from 7×10^{-11} cm^2/s to 3×10^{-9} cm^2/s. In this work, we consider following theories to explain the trends in the above plot.

a. Arrhenius behavior. The temperature dependence of the lithium ion diffusion coefficient can be modeled by the following Arrhenius equation:

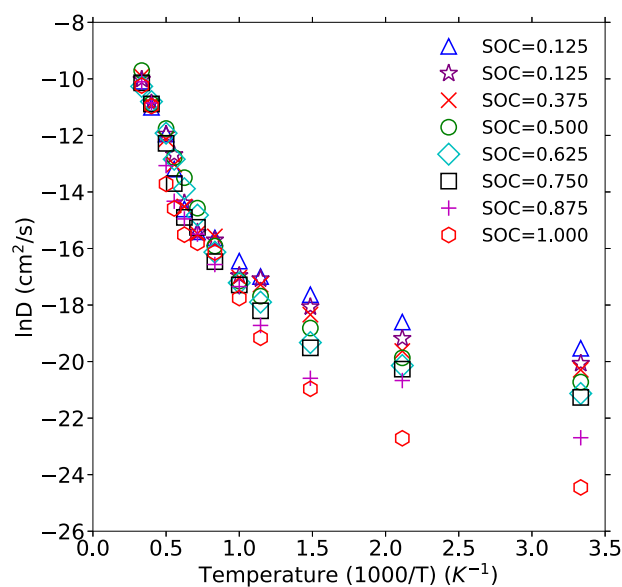$$D_{Li} = A \exp\left(-\frac{E_a}{K_B T}\right), \tag{10}$$

FIG. 10. Diffusion with temperature for each SOC values.

where A, E_a, and k_B are the pre-exponential factor, activation energy, and Boltzmann constant, respectively. It can be seen from Eq. (10) that the diffusivity of the ions can increase with an increase in temperature or when the activation energy is lower. Assuming constant values for the pre-exponential factor and the activation energy in Eq. (10), we will obtain a linear relationship between ln D and 1000/T. In doing so, following the proposition of Kuwata et al.,[19] if we split the temperature region into a high temperature zone (T > 823 K) and a low temperature zone (473 K < T < 823 K), we can observe two distinct slopes corresponding to the different activation energies in Fig. 11. This could be an indicator that the MD simulations are able to capture the vacancy diffusion mechanism in the near stoichiometric material.[46] According to the vacancy diffusion mechanism, for an ion to diffuse without an available vacant site, the total required activation energy will be the sum of vacancy formation and migration energy. This total activation energy can be written as

$$E_a = E_a^{VF} + E_a^{VM}, \qquad (11)$$

where E_a^{VF} and E_a^{VM} are activation energies for vacancy formation and migration, respectively. Total activation energy can be calculated using Eq. (11). In the stoichiometric $LiMn_2O_4$, all the lithium (8a) sites are occupied, and therefore, a small number of Li vacancies govern the lithium ion diffusion. As per the vacancy diffusion theory, it can be divided into two regions, high temperature intrinsic and low temperature extrinsic. Kuwata et al.[19] have prescribed the enthalpy of vacancy formation and migration energy for ionic diffusion as 0.6 eV and 0.5 eV, respectively. At the high temperature intrinsic region, total activation for vacancy formation and migration can be obtained so that the lithium ion can easily

diffuse. However, in the low temperature extrinsic region, to calculate the diffusion coefficient, a vacancy has been created by extracting a lithium ion from the system. Hence, only migration energy would be required to start the diffusion. Therefore, the total activation energy in the Arrhenius equation will be reduced to only migration energy along with a new pre-exponential factor.

As shown in Fig. 11, based on our data, the vacancy formation and migration energies are ~0.59 eV and 0.42 eV, respectively. In other words, the results from the MD simulations of this work follow a similar trend with experimental results. However, the required migration energy is somewhat under-predicted, and this could be due to the fact that we have used the optimum structure configuration where ions might have different migration paths.

b. Enhanced-Arrhenius behavior. While the above Arrhenius behavior explains the trends in the molecular dynamics data to a large extent, from Fig. 10, it is clear that the data are not completely linear. At higher temperatures, especially near the transition zone, the activation energy along with the pre-exponential factor can change with temperature. Hence, it would not be ideal to assume that the activation energy is independent of temperature.[47] The disagreements of the diffusion coefficients with the Arrhenius trend through the entire range of temperature considered in this work could be attributed to the variations in the activation energy and pre-exponential factor with temperature. To accommodate this variation, we assume a linear variation of activation energy and the pre-exponential factor in the range [0.3 eV, 1.7 eV] and [1×10^{-7} cm²/s, 0.025 cm²/s], respectively. The extreme values in these ranges are similar to the values proposed by Kuwata et al.[19] Specifically, we propose the following linear equations for A and E_a:

$$A = A_0 + \Delta A \frac{T - T_0}{T_{high} - T_{low}}, \qquad (12)$$

$$E_a = E_{a0} + \Delta E_a \frac{T - T_0}{T_{high} - T_{low}}. \qquad (13)$$

In Eqs. (12) and (13), T_{high} and T_{low} are the highest and lowest temperature point of the particular fitted curve line. A_0, E_{a0}, and T_0 are the reference pre-exponential factor, activation energy, and temperature, respectively. Table III shows the values of constants for both fitted curve lines.

As shown in Fig. 12, the fitted curve is in good agreement with the simulation generated data points except the temperature between 1200 K and 2000 K.

c. Volmer–Fulcher–Tammann hypothesis. In another study by Bauer et al.,[48] while investigating the molecular dynamics near the transition temperature, the authors found that there are deviations from the Arrhenius law. We believe that the trends found by them, although for a different application, are probably relevant in this work for higher temperature zones. More precisely, we can observe that the trends in Fig. 10 seem to follow the Volmer–Fulcher–Tammann (VFT) hypothesis.[49] In this theory, the diffusion
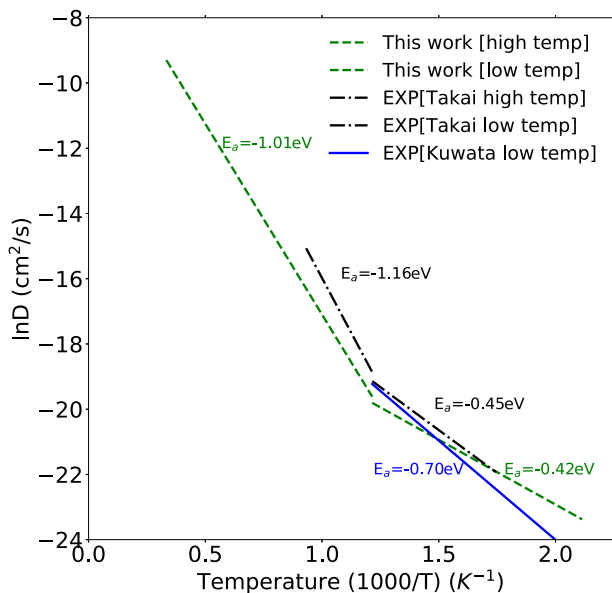
FIG. 11. Arrhenius trend for the variation of diffusion coefficient with temperature at SOC = 1.

TABLE III. Values of the parameters in Eqs. (12) and (13).

Curve zone	A_0 (cm^2/s)	E_{a0} (eV)	T_0 (K)	T_{high} (K)	T_{low} (K)	ΔA (cm^2/s)	ΔE_a (eV)
High temperature	0.005	1.01	823	3000	823	0.02	0.69
Low temperature	1×10^{-6}	0.42	823	823	323	9×10^{-6}	0.12

coefficient below and above a certain transition temperature can be represented as[50]

$$D_{\text{Li}} = A \exp\left(-\frac{B}{(T - T_{VFT})}\right), \quad (14)$$

where A, B, and T_{VFT} are fitting parameters denoted as the pre-factor, VFT-activation energy, and VFT-temperature, respectively. According to the VFT hypothesis, the non-Arrhenius behavior of diffusivity is observed in the under-cooled state.[51–54] During supercooling, a rapid increase in the high energetic favorable local clusters can cause less mobility of the ions.[55] Thus, the hypothesis suggests that the pre-factor and VFT-activation energy are dependent on the temperature, similar to our observations in the enhanced-Arrhenius formulation. Additionally, the VFT-temperature (T_{VFT}) is also needed to calculate the diffusion coefficient. However, at this time, due to the lack of experimental data for this material at the molecular level, it would be difficult to validate this theory. Hence, understanding that the experimental validation is critical, a detailed study on the non-Arrhenius behavior of the diffusivity has not been performed in this work. However, our results clearly show that it would be an interesting research to follow up in the future.
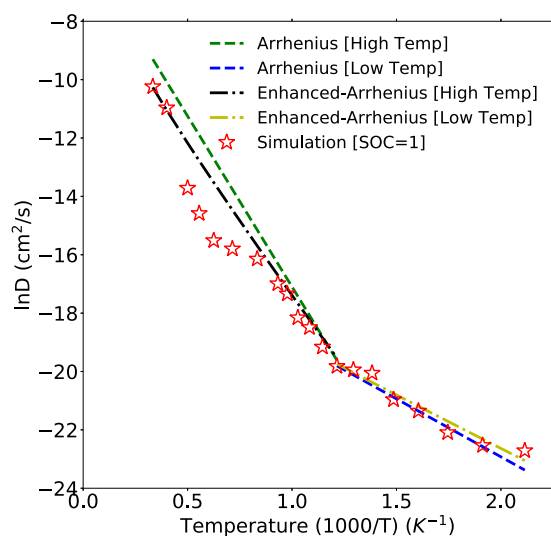
FIG. 12. Arrhenius and enhanced-Arrhenius trends for the variation of the diffusion coefficient with temperature at SOC = 1.

IV. CONCLUSION

In order to understand the intercalation induced effect on mechanical properties of the Li$_x$Mn$_2$O$_4$ cathode material for lithium ion batteries, a series of molecular dynamics simulations were performed. The computational tool was validated with respect to the experimental data by calculating the lattice parameter for the optimized LiMn$_2$O$_4$. It was found that during full discharging cycle, the lattice constant varies from 8.042 Å to 8.235 Å, which is in very good agreement with the experimental data. The total lattice and volume change during the charging cycle were 2.34% and 6.87%, respectively, which is also in very good agreement with the experimental data.

The validated computational tool was used to conduct a parametric study on the effect of state of charge, strain rate, and temperature on the performance of the battery. Results are validated with the experimental data available from the literature. It has been noticed that an increase in SOC values (Lithium content) causes higher ultimate stress that is due to less number of defects in the crystal structure. Furthermore, Young's modulus for different SOC values is consistent with the literature. The stress–strain curve does not differ much for the fully discharged state (LiMn$_2$O$_4$). However, a higher strain rate tends to initiate the fracture mechanism earlier in the intermediate charging states. In general, the strain-rate simulations illustrate higher yield stress and ultimate stress for a slower strain rate, especially for intermediate SOC values. A study of the diffusion process found that at room temperature, the diffusion coefficient increases by nearly two orders of magnitude from a fully charged state to a fully discharged state. Furthermore, temperature dependency analysis suggests that the diffusion coefficient follows the Arrhenius diffusion equation. The results are consistent with the theory on the vacancy diffusion mechanism. Consistent with the propositions in the literature, accounting for a change in the activation energy in the two temperature zones enhances the accuracy of the model in capturing the diffusion processes more accurately. This also suggests that the diffusion coefficient at lower temperatures such as 473 K and 300 K is higher than expected from just migration activation energy extrapolation but is closer to the actual diffusion coefficient. To describe the trends in the diffusion coefficient more accurately, we also propose the enhanced-Arrhenius formalism in which a temperature dependent activation energy and pre-constant result in a better fit with the molecular dynamics data. We believe that this temperature dependence could also potentially be explained by the VFT theory.

AUTHORS' CONTRIBUTIONS

All authors contributed equally to this work.

DATA AVAILABILITY

The data that support the findings of this study are available from the corresponding author upon reasonable request.

REFERENCES

[1] A. Manthiram, "Materials challenges and opportunities of lithium ion batteries," J. Phys. Chem. Lett. **2**, 373 (2011).

[2] H. Xia, Z. Luo, and J. Xie, "Nanostructured $LiMn_2O_4$ and their composites as high-performance cathodes for lithium-ion batteries," Prog. Nat. Sci.: Mater. Int. **22**, 572 (2012).

[3] E. Iguchi, Y. Tokuda, H. Nakatsugawa, and F. Munakata, "Electrical transport properties in $LiMn_2O_4$, $Li_{0.95}Mn_2O_4$, and $LiMn_{1.95}B_{0.05}O_4$ (B =Al or Ga) around room temperature," J. Appl. Phys. **91**, 2149 (2002).

[4] S. Y. Luchkin, K. Romanyuk, M. Ivanov, and A. L. Kholkin, "Li transport in fresh and aged $LiMn_2O_4$ cathodes via electrochemical strain microscopy," J. Appl. Phys. **118**, 072016 (2015).

[5] R. Sharma, N. Sharma, and M. Sharma, "$LiMn_2O_4$ spinel structure as cathode material for Li-ion batteries," AIP Conf. Proc. **2142**, 040024 (2019).

[6] H.-Y. Amanieu, M. Aramfard, D. Rosato, L. Batista, U. Rabe, and D. C. Lupascu, "Mechanical properties of commercial $Li_xMn_2O_4$ cathode under different state of charge," Acta Mater. **89**, 153–162 (2015).

[7] J. Tarascon and M. Armand, "Issues and challenges facing rechargeable lithium batteries," Nature **414**, 359 (2001).

[8] J. Cabana, T. Valdés-Solís, M. Palacín, J. Oró-Solé, A. Fuertes, G. Marbán, and A. Fuertes, "Enhanced high rate performance of $LiMn_2O_4$ spinel nanoparticles synthesized by a hard-template route," J. Power Sources **166**, 492 (2007).

[9] C. Julien, A. Mauger, A. Vijh, and K. Zaghib, *Lithium Batteries: Science and Technology* (Springer International Publishing, 2016).

[10] J. T. K. Newman, H. Hafezi, and D. R. Wheeler, "Modelling of lithium-ion batteries," J. Power Sources **119-121**, 838–843 (2003).

[11] J. Christensen and J. Newman, "A mathematical model of stress generation and fracture in lithium manganese oxide," J. Electrochem. Soc. **153**, A1019 (2006).

[12] W. H. Woodford, Y.-M. Chiang, and W. C. Carter, "'Electrochemical shock' of intercalation electrodes: A fracture mechanics analysis," J. Electrochem. Soc. **157**, A1052–A1059 (2010).

[13] Y. Hu, X. Zhao, and Z. Suo, "Averting cracks caused by insertion reaction in lithium-ion batteries," J. Mater. Res. **25**, 1007 (2010).

[14] X. Zhang, W. Shyy, and A. M. Sastry, "Numerical simulation of intercalation-induced stress in Li-ion battery electrode particles," J. Electrochem. Soc. **154**, A910 (2007).

[15] X. Zhang, A. M. Sastry, and W. Shyy, "Intercalation-induced stress and heat generation within single lithium-ion battery cathode particles," J. Electrochem. Soc. **155**, A542 (2008).

[16] J. Christensen, "Modeling diffusion-induced stress in Li-ion cells with porous electrodes," J. Electrochem. Soc. **157**, A366 (2010).

[17] J. Park, W. Lu, and A. M. Sastry, "Numerical simulation of stress evolution in lithium manganese dioxide particles due to coupled phase transition and intercalation," J. Electrochem. Soc. **158**, A201–A206 (2011).

[18] M. Y. Saidi, J. Barker, and R. Koksban, "Thermodynamic and kinetic investigation of lithium insertion in the $Li_{1-x}Mn_2O_4$ spinel phase," J. Solid State Chem. **122**, 195–199 (1996).

[19] N. Kuwata, M. Nakane, T. Miyazaki, and K. Mitsuishi, "Lithium diffusion coefficient in $LiMn_2O_4$ thin films measured by secondary ion mass spectrometry with ion-exchange method," Solid State Ionics **320**, 266–271 (2018).

[20] S. Takai, K. Yoshioka, H. Iikura, M. Matsubayashi, T. Yao, and T. Esaka, "Tracer diffusion coefficients of lithium ion in $LiMn_2O_4$ measured by neutron radiography," Solid State Ionics **256**, 93 (2014).

[21] B. V. Merinov, S. Naserifar, S. V. Zybin, S. Morozov, W. A. Goddard, J. Lee, J. H. Lee, H. E. Han, Y. C. Choi, and S. H. Kim, "Li-diffusion at the interface between Li-metal and $[Pyr_{14}][TFSI]$-ionic liquid: *Ab initio* molecular dynamics simulations," J. Chem. Phys. **152**, 031101 (2020).

[22] C. A. Brackley, A. N. Morozov, and D. Marenduzzo, "Models for twistable elastic polymers in Brownian dynamics, and their implementation for LAMMPS," J. Chem. Phys. **140**, 135103 (2014).

[23] J. C. Tully, "Molecular dynamics with electronic transitions," J. Chem. Phys. **93**, 1061 (1990).

[24] Y. Ida, "Interionic repulsive force and compressibility of ions," Phys. Earth Planet. Inter. **13**, 97 (1976).

[25] K. Suzuki, Y. Oumi, S. Takami, M. Kubo, A. Miyamoto, M. Kikuchi, N. Yamazaki, and M. Mita, "Structural properties of $Li_xMn_2O_4$ as investigated by molecular dynamics and density functional theory," Jpn. J. Appl. Phys., Part 1 **39**, 4318 (2000).

[26] K. Sickafus, J. Wills, and N. Grimes, "Structure of spinel," J. Am. Ceram. Soc. **82**, 3279 (2004).

[27] S. Plimpton, "Fast parallel algorithms for short-range molecular dynamics," J. Comput. Phys. **117**, 1 (1995).

[28] R. Cygan, H. Westrich, and D. Doughty, "Ionic modeling of lithium manganese spinel materials for use in rechargeable batteries," MRS Proc. **393**, 113 (1995).

[29] G. V. Lewis and C. R. A. Catlow, "Potential models for ionic oxides," J. Phys. C: Solid State Phys. **18**, 1149 (1985).

[30] P. P. Ewald, "The calculation of optical and electrostatic grid potential," Ann. Phys. **64**, 253 (1921).

[31] S. Nosé, "A unified formulation of the constant temperature molecular dynamics methods," J. Chem. Phys. **81**, 511–519 (1984).

[32] A. Subramaniyan and C. Sun, "Continuum interpretation of virial stress in molecular simulations," Int. J. Solids Struct. **45**, 4340 (2008).

[33] A. Adan, C. T. Sun, and H. Mahfuz, "A molecular dynamics simulation study to investigate the effect of filler size on elastic properties of polymer nanocomposites," Compos. Sci. Technol. **67**, 348–356 (2007).

[34] A. Grenall, "Isothermal compositional order-disorder. I. Superstructure solid solutions in a salt system," J. Chem. Phys. **17**, 1036 (1949).

[35] R. E. Garcia, Y. M. Chiang, W. C. Carter, P. Limthongkul, and C. M. Bishopb, "Microstructural modeling and design of rechargeable lithium-ion batteries," J. Electrochem. Soc. **152**, A255–A263 (2005).

[36] T. Ohzuku, M. Kitagawa, and T. Hirai, "Electrochemistry of manganese dioxide in lithium nonaqueous cell: III. X-ray diffractional study on the reduction of spinel-related manganese dioxide," J. Electrochem. Soc. **137**, 769 (1990).

[37] M. Thackeray, W. David, P. Bruce, and J. Goodenough, "Lithium insertion into manganese spinels," Mater. Res. Bull. **18**, 461 (1983).

[38] M. Chung, J. Seo, X. Zhang, and A. Sastry, "Implementing realistic geometry and measured diffusion coefficients into single particle electrode modeling based on experiments with single $LiMn_2O_4$ spinel particles," J. Electrochem. Soc. **158**, A371 (2011).

[39] E. V. Vakarin, G. G. Belmonte, and J. P. Badiali, "Interplay of host volume variations and internal distortions in the course of intercalation into disordered matrices," J. Chem. Phys. **126**, 234709 (2007).

[40] N. H. Nachtrieb, E. Catalano, and J. A. Weil, "Self-diffusion in solid sodium. I," J. Chem. Phys. **20**, 1185 (1952).

[41] S. Lee, J. Park, A. M. Sastry, and W. Lu, "Molecular dynamics simulations of SOC-dependent elasticity of $Li_xMn_2O_4$ spinels in Li-ion batteries," J. Electrochem. Soc. **160**, A968–A972 (2013).

[42] A. Asadi, S. Aghamiri, and M. Talaie, "Molecular dynamics simulation of a $Li_xMn_2O_4$ spinel cathode material in Li-ion batteries," RSC Adv. **6**, 115354 (2016).

[43] W. H. Woodford, Y.-M. Chiang, and W. C. Carter, "Electrochemical shock in ion-intercalation materials with limited solid-solubility," J. Electrochem. Soc. **160**, A1286–A1292 (2013).

[44] N. Kuwata, X. Lu, T. Miyazaki, Y. Iwai, T. Tanabe, and J. Kawamura, "Lithium diffusion coefficient in amorphous lithium phosphate thin films measured by secondary ion mass spectroscopy with isotope exchange methods," Solid State Ionics **294**, 59–66 (2016).

[45] U. Kumar, A. Metya, N. Ramakrishnan, and J. Singh, "A study of transport properties and stress analysis using atomistic and macro simulations for lithium-ion batteries," J. Electrochem. Soc. **161**, A1453 (2014).

[46] K. Hoang, "Understanding the electronic and ionic conduction and lithium over-stoichiometry in $LiMn_2O_4$ spinel," J. Mater. Chem. A **2**, 18271 (2014).

[47] A. P. Zeke, O. M. Oluwaseun, and H. T. Ward, "Activation energies and beyond," J. Phys. Chem. **123**, 7185–7194 (2019).

[48] T. Bauer, P. Lunkenheimer, and A. Loidl, "Cooperativity and the freezing of molecular motion at the glass transition," Phys. Rev. Lett. **111**, 225702 (2013).

[49] P. G. Debenedetti, *Metastable Liquids: Concepts and Principles* (Princeton University Press, 1996).

[50] R. S. Smith and B. D. Kay, "The existence of supercooled liquid water at 150 K," Nature **398**, 788–791 (1999).

[51] D. Cangialosi, A. Angel, and J. Colmenero, "On the temperature dependence of the nonexponentiality in glass-forming liquids," J. Chem. Phys. **130**, 124902 (2009).

[52] C. A. Angell, "Formation of glasses from liquids and biopolymers," Science **267**, 1924–1935 (1995).

[53] F. Faupel, W. Frank, M. Macht, H. Mehrer, V. Naundorf, K. Rätzke, S. K. Schober, H. R. andSharma, and H. Teichler, "Diffusion in metallic glasses and supercooled melts," Rev. Mod. Phys. **75**, 237 (2003).

[54] A. Pasturel, E. S. Tasci, M. H. F. Sluiter, and N. Jakse, "Structural and dynamic evolution in liquid Au-Si eutectic alloy by *ab initio* molecular dynamics," Phys. Rev. B **81**, 140202 (2010).

[55] R. Trivedi, P. Magnin, and W. Kurz, "Theory of eutectic growth under rapid solidification conditions," Acta Metall. Mater. **35**, 971–980 (1987).